

# Role of ionic electrodiffusion and ephaptic coupling in cardiac dynamics

Ning Wei <sup>1,\*</sup> and Yoichiro Mori<sup>2</sup>

<sup>1</sup>Purdue University, Department of Mathematics, 150 N. University St., West Lafayette, IN 47907.

<sup>2</sup>University of Pennsylvania, Department of Mathematics and Department of Biology, David Rittenhouse Laboratory, 209 S. 33rd St., Philadelphia, PA 19104.

\*Correspondence: wei307@purdue.edu

**ABSTRACT** Cardiac myocytes coordinate the heart contractions through electrical signaling, facilitated by gap junctions (GJs) in the intercalated disc (ID). GJs provide low-resistance pathways for electrical propagation between myocytes, acting as the main mechanism for electrical communication in the heart. However, studies show that conduction can persist in the absence of GJs. For instance, GJ knockout mice still display slow and discontinuous electrical propagation, suggesting the presence of alternative communication mechanisms. Ephaptic coupling (EpC) serves as an alternative way for cell communication, relying on electrical fields within narrow clefts between neighboring myocytes. Studies show that EpC can enhance conduction velocity (CV) and reduce conduction block (CB), especially when GJs are compromised. Reduced GJs and significant electrochemical gradients are prevalent in various heart diseases. However, existing models often fail to capture their combined influence on cardiac conduction, which limits our understanding of both the physiological and pathological aspects of the heart. Our study aims to address this gap through the development of a two-dimensional (2D) discrete multidomain electrodiffusion model that includes EpC. In particular, we investigated the interplay between EpC and multidomain electrodiffusion on action potential (AP) propagation, morphology, and electrochemical properties. Our findings indicate that under strong EpC, Na<sup>+</sup> electrodiffusion enhances CV, reduces the occurrence of CB, and sharpens the upstroke phase of the AP, while Ca<sup>2+</sup> and K<sup>+</sup> diffusion shorten the AP duration, alter the repolarization phase, and elevate the resting membrane potential. Additionally, when EpC is prominent, Na<sup>+</sup> electrodiffusion helps stabilize AP propagation and promotes its spread into ischemic regions. Strong EpC also significantly alters ionic concentrations in the cleft, markedly increasing [K<sup>+</sup>], nearly depleting [Ca<sup>2+</sup>], and causing moderate changes in [Na<sup>+</sup>]. This multidomain electrodiffusion model provides valuable insights into the mechanisms of EpC in the heart.

**SIGNIFICANCE** Our ongoing research focuses on developing a two-dimensional discrete multidomain electrodiffusion model that incorporates ephaptic coupling (EpC), aiming to create a more biologically detailed representation of ephaptic conduction in both healthy and diseased heart. This model helps us better understand the role of EpC in cardiac dynamics, particularly in diseased hearts where gap junctions are remodeled and electrochemical gradients are elevated. We investigated the interaction between ionic electrodiffusion and EpC, with particular attention to action potential propagation, morphology, and electrochemical properties in healthy and ischemic hearts. Ultimately, this work seeks to uncover the mechanisms of EpC and evaluate its potential as a protective, anti-arrhythmic mechanism in cardiac physiology.

## INTRODUCTION

Cardiac cells coordinate muscular contraction to pump blood through electrical communication. Gap junctions (GJs), located in the intercalated disc (ID) between myocytes, serve as low-resistance pathways mediating the propagation of electrical impulses in the heart (1–4). GJ was widely acknowledged as the primary mechanism for electrical communication within the heart (5). However, experimental observations from the 2000s have raised concerns regarding whether conduction can be sustained in the absence of GJs (6, 7). For instance, intercellular conductance in pairs of GJ-deficient adult rat myocytes was dramatically reduced from 588 nS to 10 nS (7). Despite this, impulse propagation was only reduced by 50%, suggesting the presence of alternative mechanisms for cell-to-cell communication in the heart.

An alternative mechanism for cardiac conduction, known as ephaptic coupling (EpC), has been proposed to explain the spread of electrical activity in the heart when GJs are compromised. Research has demonstrated that EpC is heavily dependent on the electrical fields within the narrow clefts between adjacent myocytes (8, 9). Since the mid-20th century, EpC has been the focus of ongoing experimental and computational investigations; however, direct experimental evidence of its existence remains elusive. As a result, researchers have sought to indirectly confirm EpC by investigating its physiological role under both normal and various pathological conditions (9–21). For example, studies suggest that EpC can help restore cardiac conduction when GJ is compromised. Specifically, studies have demonstrated that EpC enhances conduction velocity (CV) (11, 12, 16, 21–23), mitigates conduction block (CB) (14, 21), and ultimately terminating reentry (15) in ischemic heart models with diminished GJ.

Remodeled GJs and pronounced electrochemical gradients are common characteristics in various heart diseases, disrupting normal electrical signaling and potentially leading to arrhythmias (5, 24–31). However, existing models often overlook the combined influences of the two on cardiac dynamics, hindering our understanding of the pathological states in the heart. For example, most mathematical models of cellular electrical activity in the heart are based on the cable model, derived from a current continuity relation on a one-dimensional ohmic cable (11, 12, 22, 23, 32–34). This derivation relies on several assumptions: ionic concentrations are presumed to remain relatively stable over the time, and a one-dimensional representation of cell geometry is considered sufficient for describing electrical activity. However, these assumptions may not be valid in the heart, where microscopic features can critically influence physiological responses. In fact, recent models incorporating electrodiffusion for the heart have become available. For example, in (35), the authors incorporated the detailed geometry of ID along one-dimensional (1D) strand of coupled cells. However, they limited the electrodiffusion of  $\text{Na}^+$  between cleft and the bulk, which may conflict with the principle of electroneutrality. Indeed, if the concentration of one ion changes, it leads to changes in the ionic concentration of the rest of ions. In (13), the authors presented an electrodiffusion model that accounted for the three-dimensional (3D) geometry and ionic concentration effects along a strand of cells. Modeling a strand of cells alone (13, 35) is insufficient for considering the complexity of arrhythmias in the heart. Our study seeks to bridge this gap by developing a two dimensional (2D) discrete multidomain electrodiffusion model that incorporates EpC, which captures ion accumulation and movement at both subcellular and cellular levels. This is the first model to capture the dynamics, particularly the electrodiffusion, of all major ions across multiple domains, enabling us to reveal the impact of EpC on cardiac function and arrhythmogenesis.

In this paper, we explored the interplay between ionic electrodiffusion and EpC on cardiac dynamics, including AP propagation, morphology, and electrochemical properties in both healthy and ischemic hearts. To achieve this, we developed a 2D discrete multidomain electrodiffusion model that incorporates EpC. Our findings indicate that under strong EpC,  $\text{Na}^+$  electrodiffusion enhances CV, reduces the occurrence of CB, and sharpens the upstroke phase of the AP, while  $\text{Ca}^{2+}$  and  $\text{K}^+$  diffusion shorten the AP duration, alter the repolarization phase, and elevate the resting membrane potential. Additionally, when EpC is prominent,  $\text{Na}^+$  electrodiffusion helps stabilize AP propagation and promotes its spread into ischemic regions. Strong EpC also significantly alters ionic concentrations in the cleft, markedly increasing  $[\text{K}^+]$ , nearly depleting  $[\text{Ca}^{2+}]$ , and causing moderate changes in  $[\text{Na}^+]$ . This multidomain electrodiffusion model provides valuable insights into the mechanisms of EpC in the heart.

## MATERIALS AND METHODS

### Overview

In this section, we aim to develop a 2D discrete multidomain electrodiffusion model with EpC. Fig. 1 (left) illustrates the lattice view of the model, where each cell is represented as a cylinder, and the cells are interconnected by GJs to form an  $M \times N$  rectangular lattice. At each lattice point  $(i, j)$ , we assigned electrochemical pairs for intracellular ( $\phi_i^{(i,j)}, C_i^{(i,j)}$ ) and extracellular ( $\phi_e^{(i,j)}, C_e^{(i,j)}$ ) spaces to track the variations in both potential and ionic concentrations of  $\text{Na}^+$ ,  $\text{K}^+$ ,  $\text{Ca}^{2+}$ , and  $\text{Cl}^-$ . The cleft space is located between cells  $(i, j)$  and  $(i, j + 1)$ . We then defined a cleft potential  $\phi_c^{(i,j+\frac{1}{2})}$  and concentrations  $C_c^{(i,j+\frac{1}{2})}$  of the four ions at the location  $(i, j + \frac{1}{2})$ . The space within the extracellular region, adjacent to the cleft, is referred to as the extracellular-cleft space. The potential and ionic concentrations in the extracellular-cleft space are denoted by  $\phi_{ec}^{(i,j+\frac{1}{2})}$  and  $C_{ec}^{(i,j+\frac{1}{2})}$ , respectively.

Fig. 1 (right) illustrates the connection between lattices. Specifically, it depicts a circuit diagram for two adjacent cells that are ephaptically coupled through a shared cleft space, with end-to-end gap junctions ( $GJ_{\text{end}}$ ). Side-to-side gap junctions ( $GJ_{\text{side}}$ ) and diffusive ionic flows between extracellular spaces, regulated by  $R_{ee}$  in the transverse direction, are not shown here. The cleft space was modeled as a single narrow compartment, resistively coupled ( $R_c$ ) to the extracellular-cleft space through diffusive ionic flows. Communication between extracellular spaces in the longitudinal direction occurs through the shared extracellular-cleft space, which involves diffusive ionic flows between the extracellular and extracellular-cleft spaces, regulated

by  $R_{ec}$ . Intracellular and extracellular spaces in each cell are separated by the cell side membrane, while intracellular and cleft spaces are separated by the cell end membrane. Both the side and end membranes allow the free flow of ionic and capacitive currents. To minimize computational costs, we treated each space as isopotential and assumed uniform concentrations within it.

## Modeling multidomain electrodiffusion

Electrodiffusion is a passive process by which charged particles are transported between cardiac cells under the influence of two simultaneously acting forces, namely, the gradients of particle density and electric potential. We applied Goldman-Hodgkin-Katz (GHK) equation (below) to describe the ionic current labeled by  $k$  across cell membrane, which is a function of the transmembrane potential ( $V_m$ ) and the ionic concentrations inside ( $C_{i,k}$ ) and outside ( $C_{e,k}$ ) of the cell:

$$I(P_k, C_{i,k}, C_{e,k}, V_i, V_e) = P_k \frac{z_k^2 F^2}{RT} (V_i - V_e) \frac{C_{i,k} - C_{e,k} \exp\left(-\frac{z_k F (V_i - V_e)}{RT}\right)}{1 - \exp\left(-\frac{z_k F (V_i - V_e)}{RT}\right)},$$

where  $P_k$  represents the permeability of the membrane for ion  $k$  and  $z_k$  denotes its charge valance. The index  $k$  refers to the four major ionic species:  $\text{Na}^+$ ,  $\text{K}^+$ ,  $\text{Ca}^{2+}$  and  $\text{Cl}^-$ .  $R$ ,  $T$ , and  $F$  are the ideal gas constant, absolute temperature and Faraday's constant, respectively.

Here, we modeled multiple ion electrodiffusion between four domains. In particular, we modeled the electrodiffusion between intracellular spaces; between cleft and extracellular-cleft spaces; between extracellular and extracellular-cleft spaces; and between extracellular spaces in the vertical direction. For each domain, we tracked the potential ( $\phi_i$ ,  $\phi_e$ ,  $\phi_c$ ,  $\phi_{ec}$ ) and concentration ( $C_{i,k}$ ,  $C_{e,k}$ ,  $C_{c,k}$ ,  $C_{ec,k}$ ) of each ion. The ionic fluxes between domains are described by GHK flux equation, in which the movement of ions is tightly coupled to the electrochemical gradient.

## Modeling EpC

EpC is strongly dependent on the presence of the cleft space between the ends of adjacent cells. This cleft space communicates with the end membranes of neighboring cells and the extracellular space independently. We modeled EpC by considering the active end membranes linked through a shared cleft potential, along with the dynamic interaction between the cleft and the extracellular space via a high-resistance ( $R_c$ ) diffusion process.  $R_c$  is inversely proportional to the cleft width ( $d_{\text{cleft}}$ ), with the corresponding formula provided in Table A1 of (23) and Table 1 of (21). We selected the values of  $d_{\text{cleft}}$  ranging from 4 nm to 115 nm to represent the different levels of EpC, which are governed by  $R_c$ . A smaller  $d_{\text{cleft}}$  corresponds to a larger  $R_c$ , indicating a significantly stronger EpC, whereas a sufficiently large  $d_{\text{cleft}}$  signifies the near absence of EpC.

In contrast to our previous work (14, 15, 21), where ionic electrodiffusion was not included, this study tracks the dynamics of  $\text{Na}^+$ ,  $\text{K}^+$ ,  $\text{Ca}^{2+}$ , and  $\text{Cl}^-$  within the cleft. The movement of these ions are influenced by the combined effects of ionic flux across the opposing end membranes and the diffusive flux between the cleft and the extracellular space, which is regulated by the electrochemical gradient established between the two.

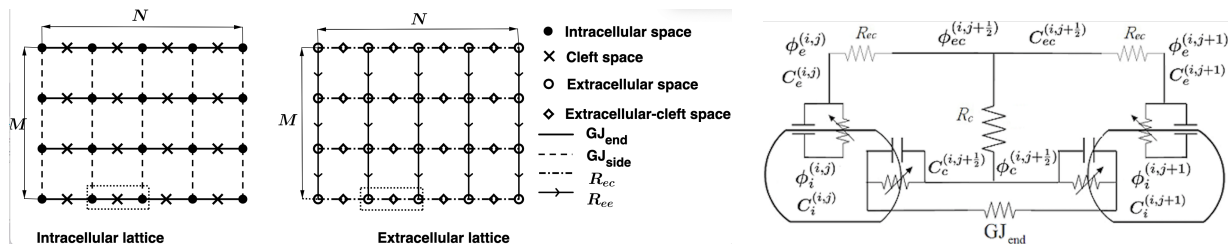


Figure 1: A lattice view of our 2D discrete multidomain electrodiffusion model (left) and a circuit diagram for two adjacent cells coupled through a shared single (middle) compartment cleft in the presence of electrodiffusion and end-to-end GJs ( $GJ_{\text{end}}$ , right).

The model equations presented below were derived based on the principles of current balance and concentration conservation for each domain and ion ( $k = 1 \sim 4$  represents  $\text{Na}^+$ ,  $\text{K}^+$ ,  $\text{Ca}^{2+}$ , and  $\text{Cl}^-$ ). All parameters are drawn from the references (14, 15, 21). Specifically, the current balance refers to the equilibrium among capacitive currents ( $C_m \frac{\partial \phi}{\partial t}$ ), ionic currents ( $I_{\text{side}}$  and  $I_{\text{end}}$ ), and electrodiffusive currents between different domains (GHK currents). This is a discretized version of the Poisson-Nernst-Planck (PNP) equation, where the discreteness of the model offers a more precise representation of the discontinuous conduction observed during myocardial ischemia.

**Intracellular space** ( $\phi_i^{(i,j)}$ ,  $C_{i,k}^{(i,j)}$ ):

$$\begin{aligned}
 & \sum_{k=1}^4 A_{\text{end}} I(P_{\text{GJ},k}^{\text{end}}, C_{i,k}^{(i,j)}, C_{i,k}^{(i,j+1)}, \phi_i^{(i,j)}, \phi_i^{(i,j+1)}) + \sum_{k=1}^4 A_{\text{end}} I(P_{\text{GJ},k}^{\text{end}}, C_{i,k}^{(i,j)}, C_{i,k}^{(i,j-1)}, \phi_i^{(i,j)}, \phi_i^{(i,j-1)}) \\
 & + \sum_{k=1}^4 \frac{A_{\text{side}}}{2} I(P_{\text{GJ},k}^{\text{side}}, C_{i,k}^{(i,j)}, C_{i,k}^{(i+1,j)}, \phi_i^{(i,j)}, \phi_i^{(i+1,j)}) + \sum_{k=1}^4 \frac{A_{\text{side}}}{2} I(P_{\text{GJ},k}^{\text{side}}, C_{i,k}^{(i,j)}, C_{i,k}^{(i-1,j)}, \phi_i^{(i,j)}, \phi_i^{(i-1,j)}) \\
 & + A_{\text{end}} C_m \frac{\partial(\phi_i^{(i,j)} - \phi_c^{(i,j+\frac{1}{2})})}{\partial t} + A_{\text{end}} C_m \frac{\partial(\phi_i^{(i,j)} - \phi_c^{(i,j-\frac{1}{2})})}{\partial t} + A_{\text{end}} I_{\text{end}}^{R,L} + A_{\text{side}} C_m \frac{\partial(\phi_i^{(i,j)} - \phi_e^{(i,j)})}{\partial t} + A_{\text{side}} I_{\text{side}} = 0,
 \end{aligned} \tag{1}$$

$$\begin{aligned}
 v_i \frac{\partial C_{i,k}^{(i,j)}}{\partial t} = & -A_{\text{end}} \frac{I(P_{\text{GJ},k}^{\text{end}}, C_{i,k}^{(i,j)}, C_{i,k}^{(i,j+1)}, \phi_i^{(i,j)}, \phi_i^{(i,j+1)})}{z_k F} - A_{\text{end}} \frac{I(P_{\text{GJ},k}^{\text{end}}, C_{i,k}^{(i,j)}, C_{i,k}^{(i,j-1)}, \phi_i^{(i,j)}, \phi_i^{(i,j-1)})}{z_k F} \\
 & - \frac{A_{\text{side}}}{2} \frac{I(P_{\text{GJ},k}^{\text{side}}, C_{i,k}^{(i,j)}, C_{i,k}^{(i+1,j)}, \phi_i^{(i,j)}, \phi_i^{(i+1,j)})}{z_k F} - \frac{A_{\text{side}}}{2} \frac{I(P_{\text{GJ},k}^{\text{side}}, C_{i,k}^{(i,j)}, C_{i,k}^{(i-1,j)}, \phi_i^{(i,j)}, \phi_i^{(i-1,j)})}{z_k F} \\
 & - A_{\text{end}} \frac{I_{\text{end}}^{R,L,k}}{z_k F} - A_{\text{side}} \frac{I_{\text{side}}^k}{z_k F} \quad (k = 1 \sim 4),
 \end{aligned} \tag{2}$$

where  $P_{\text{GJ},k}^{\text{end}}$  and  $P_{\text{GJ},k}^{\text{side}}$  represent the permeability of end-to-end and side-to-side GJs to the ion  $k$ ;  $z_k$  denotes the ionic valence (+1 for  $\text{Na}^+$  and  $\text{K}^+$ , +2 for  $\text{Ca}^{2+}$ , -1 for  $\text{Cl}^-$ );  $R$ ,  $T$ , and  $F$  are the ideal gas constant, absolute temperature, and Faraday's constant, respectively;  $A_{\text{end}}$  and  $A_{\text{side}}$  refer to the cross-sectional and side areas of a cell, respectively;  $\phi_i^{(i,j)}$ ,  $\phi_i^{(i,j-1)}$ , and  $\phi_i^{(i,j+1)}$  denote the intracellular potentials of cells  $(i, j)$ ,  $(i, j-1)$ , and  $(i, j+1)$ , respectively;  $C_{i,k}^{(i,j)}$ ,  $C_{i,k}^{(i,j-1)}$ , and  $C_{i,k}^{(i,j+1)}$  represent the intracellular concentrations of ion  $k$  in the cells  $(i, j)$ ,  $(i, j-1)$ , and  $(i, j+1)$ , respectively;  $\phi_i^{(i-1,j)}$  and  $\phi_i^{(i+1,j)}$  represent the intracellular potentials of cells  $(i-1, j)$  and  $(i+1, j)$ , respectively;  $C_{i,k}^{(i-1,j)}$  and  $C_{i,k}^{(i+1,j)}$  represent the intracellular concentrations of ion  $k$  in cells  $(i-1, j)$  and  $(i+1, j)$ , respectively;  $\phi_c^{(i,j-\frac{1}{2})}$  and  $\phi_c^{(i,j+\frac{1}{2})}$  denote cleft potentials at positions  $(i, j-\frac{1}{2})$  and  $(i, j+\frac{1}{2})$ , respectively;  $C_m$  is the membrane capacitance per unit area;  $I_{\text{end}}$  and  $I_{\text{side}}$  represent the outward ionic current density at the end and side membranes, respectively;  $\phi_e^{(i,j)}$  is the extracellular potential of cell  $(i, j)$ ;  $v_i$  denotes the cell volume. For  $k = 4$ , the terms  $\frac{I_{\text{end}}^k}{z_k F}$  and  $\frac{I_{\text{side}}^k}{z_k F}$  are omitted from Eq. (2).

**Extracellular space** ( $\phi_e^{(i,j)}$ ,  $C_{e,k}^{(i,j)}$ ):

$$\begin{aligned}
 & \sum_{k=1}^4 A_{ec} I(P_{ec,k}, C_{e,k}^{(i,j)}, C_{ec,k}^{(i,j+\frac{1}{2})}, \phi_e^{(i,j)}, \phi_{ec}^{(i,j+\frac{1}{2})}) + \sum_{k=1}^4 A_{ec} I(P_{ec,k}, C_{e,k}^{(i,j)}, C_{ec,k}^{(i,j-\frac{1}{2})}, \phi_e^{(i,j)}, \phi_{ec}^{(i,j-\frac{1}{2})}) \\
 & + \sum_{k=1}^4 \frac{A_{ee}}{2} I(P_{ee,k}, C_{e,k}^{(i,j)}, C_{e,k}^{(i+1,j)}, \phi_e^{(i,j)}, \phi_e^{(i+1,j)}) + \sum_{k=1}^4 \frac{A_{ee}}{2} I(P_{ee,k}, C_{e,k}^{(i,j)}, C_{e,k}^{(i-1,j)}, \phi_e^{(i,j)}, \phi_e^{(i-1,j)}) \\
 & - A_{\text{side}} C_m \frac{\partial(\phi_i^{(i,j)} - \phi_e^{(i,j)})}{\partial t} - A_{\text{side}} I_{\text{side}} = 0,
 \end{aligned} \tag{3}$$

$$\begin{aligned}
 v_e \frac{\partial C_{e,k}^{(i,j)}}{\partial t} = & -A_{ec} \frac{I(P_{ec,k}, C_{e,k}^{(i,j)}, C_{ec,k}^{(i,j+\frac{1}{2})}, \phi_e^{(i,j)}, \phi_{ec}^{(i,j+\frac{1}{2})})}{z_k F} - A_{ec} \frac{I(P_{ec,k}, C_{e,k}^{(i,j)}, C_{ec,k}^{(i,j-\frac{1}{2})}, \phi_e^{(i,j)}, \phi_{ec}^{(i,j-\frac{1}{2})})}{z_k F} \\
 & - \frac{A_{ee}}{2} \frac{I(P_{ee,k}, C_{e,k}^{(i,j)}, C_{e,k}^{(i+1,j)}, \phi_e^{(i,j)}, \phi_e^{(i+1,j)})}{z_k F} - \frac{A_{ee}}{2} \frac{I(P_{ee,k}, C_{e,k}^{(i,j)}, C_{e,k}^{(i-1,j)}, \phi_e^{(i,j)}, \phi_e^{(i-1,j)})}{z_k F} \\
 & + A_{\text{side}} \frac{I_{\text{side}}^k}{z_k F} \quad (k = 1 \sim 4),
 \end{aligned} \tag{4}$$

where  $A_{ec}$  and  $A_{ee}$  represent the areas of the extracellular-cleft and extracellular spaces, respectively.  $P_{ec,k}$  denotes the permeability of the ion  $k$  through the resistive connection between the extracellular space and the extra-cleft space, facilitated

by diffusive ionic flows.  $P_{e,k}$  represents the permeability of the ion  $k$  through the resistive connection between extracellular spaces in the transverse direction, facilitated by diffusive ionic flows. The extracellular potentials of cells  $(i, j)$ ,  $(i - 1, j)$ , and  $(i + 1, j)$  are denoted by  $\phi_e^{(i,j)}$ ,  $\phi_e^{(i-1,j)}$ , and  $\phi_e^{(i+1,j)}$ , respectively. Similarly, the extracellular concentrations of ion  $k$  for cells  $(i, j)$ ,  $(i - 1, j)$ , and  $(i + 1, j)$  are represented by  $C_{e,k}^{(i,j)}$ ,  $C_{e,k}^{(i-1,j)}$ , and  $C_{e,k}^{(i+1,j)}$ , respectively. The extracellular-cleft potentials at locations  $(i, j - \frac{1}{2})$  and  $(i, j + \frac{1}{2})$  are denoted by  $\phi_{ec}^{(i,j-\frac{1}{2})}$  and  $\phi_{ec}^{(i,j+\frac{1}{2})}$ , respectively, while  $C_{ec,k}^{(i,j-\frac{1}{2})}$  and  $C_{ec,k}^{(i,j+\frac{1}{2})}$  represent the extracellular-cleft concentrations of ion  $k$  at those locations. Additionally,  $v_e$  is the volume of the extracellular space. For  $k = 4$ , the term  $\frac{I_{side}^k}{z_k F}$  is omitted from Eq. (4).

**Cleft space** ( $\phi_c^{(i,j+\frac{1}{2})}$ ,  $C_{c,k}^{(i,j+\frac{1}{2})}$ ):

$$\sum_{k=1}^4 A_c I(P_{c,k}, C_{c,k}^{(i,j+\frac{1}{2})}, C_{ec,k}^{(i,j+\frac{1}{2})}, \phi_c^{(i,j+\frac{1}{2})}, \phi_{ec}^{(i,j+\frac{1}{2})}) - A_{end} C_m \frac{\partial(\phi_i^{(i,j+1)} - \phi_c^{(i,j+\frac{1}{2})})}{\partial t} - A_{end} C_m \frac{\partial(\phi_i^{(i,j)} - \phi_c^{(i,j+\frac{1}{2})})}{\partial t} - A_{end} I_{end}^{R,L} = 0, \quad (5)$$

$$v_c \frac{\partial C_{c,k}^{(i,j+\frac{1}{2})}}{\partial t} = -A_c \frac{I(P_{c,k}, C_{c,k}^{(i,j+\frac{1}{2})}, C_{ec,k}^{(i,j+\frac{1}{2})}, \phi_c^{(i,j+\frac{1}{2})}, \phi_{ec}^{(i,j+\frac{1}{2})})}{z_k F} + A_{end} \frac{I_{end}^{R,L:k}}{z_k F} \quad (k = 1 \sim 4), \quad (6)$$

where  $A_c$  represents the area of the cleft space;  $P_{c,k}$  is the permeability of the ion  $k$  through the resistive connection between the cleft space and extracellular-cleft space, mediated by diffusive ionic flows;  $v_c$  denotes the volume of cleft space. For  $k = 4$ , term  $\frac{I_{end}^k}{z_k F}$  is dropped from Eq. (6).

**Extracellular-cleft space** ( $\phi_{ec}^{(i,j+\frac{1}{2})}$ ,  $C_{ec,k}^{(i,j+\frac{1}{2})}$ ):

$$-\sum_{k=1}^4 A_c I(P_{c,k}, \phi_c^{(i,j+\frac{1}{2})}, \phi_{ec}^{(i,j+\frac{1}{2})}, C_{c,k}^{(i,j+\frac{1}{2})}, C_{ec,k}^{(i,j+\frac{1}{2})}) - \sum_{k=1}^4 A_{ec} I(P_{ec,k}, \phi_e^{(i,j+1)}, \phi_{ec}^{(i,j+\frac{1}{2})}, C_{e,k}^{(i,j+1)}, C_{ec,k}^{(i,j+\frac{1}{2})}) - \sum_{k=1}^4 A_{ec} I(P_{ec,k}, \phi_e^{(i,j)}, \phi_{ec}^{(i,j+\frac{1}{2})}, C_{e,k}^{(i,j)}, C_{ec,k}^{(i,j+\frac{1}{2})}) = 0, \quad (7)$$

$$v_{ec} \frac{\partial C_{ec,k}^{(i,j+\frac{1}{2})}}{\partial t} = A_c \frac{I(P_{c,k}, \phi_c^{(i,j+\frac{1}{2})}, \phi_{ec}^{(i,j+\frac{1}{2})}, C_{c,k}^{(i,j+\frac{1}{2})}, C_{ec,k}^{(i,j+\frac{1}{2})})}{z_k F} + \frac{A_{ec} I(P_{ec,k}, \phi_e^{(i,j+1)}, \phi_{ec}^{(i,j+\frac{1}{2})}, C_{e,k}^{(i,j+1)}, C_{ec,k}^{(i,j+\frac{1}{2})})}{z_k F} + A_{ec} \frac{I(P_{ec,k}, \phi_e^{(i,j)}, \phi_{ec}^{(i,j+\frac{1}{2})}, C_{e,k}^{(i,j)}, C_{ec,k}^{(i,j+\frac{1}{2})})}{z_k F} \quad (k = 1 \sim 4), \quad (8)$$

where  $v_{ec}$  is the volume of the extra-cellular space.

## Membrane dynamics

To provide a physiological description of the side ( $I_{side}$ ) and end membrane ( $I_{end}$ ) currents, we employed the Luo-Rudy dynamic model 2007 (LRd2007) (36). To simplify the numerical simulation of this complex system, which involves multidomain electrodiffusion of multiple ions, we did not model the calcium handling processes within the sarcoplasmic reticulum (SR) in each cell. However, we retained essential calcium-related currents, including the L-type calcium current (ICaL), background calcium current (ICab), sarcoplasmic calcium pump current (IPCa), sodium-calcium exchange current (INaCa), and transient outward calcium current (ICat).

Additionally, we modeled the *individual* localization of fast sodium (INa), L-type calcium (ICaL), and inward rectifier potassium (IKi) channels at the end membrane, based on experimental observations (37–41). This approach is crucial for investigating the distinct effects of each channel type on cardiac dynamics and for gaining insights into the mechanisms of EpC. The localization was implemented by redistributing the channels across the end membrane while keeping the total number of channels—or equivalently, the total conductance—constant. In particular, we considered three distribution scenarios: (1) localized INa with uniform ICaL and IKi; (2) localized ICaL with uniform INa and IKi; (3) localized IKi with uniform INa and ICaL. Other ionic channels are uniformly distributed, with their gating variables functioning independently on the side and end membranes.

## Modeling ischemic region

We modeled myocardial ischemia by defining three regions: the normal zone (NZ, yellow), the ischemic core (IC, blue), and the border zone (BZ), as shown in Fig.2. The BZ features a finger-like geometry, with the IC protruding into the NZ—consistent with structures observed in optical coherence tomography (OCT) data (42). We applied methods from (43, 44) to model the key features of regional acute ischemia—which typically lasts 10–15 minutes—including hyperkalemia, acidosis, anoxia, and GJ remodeling (45, 46). Hyperkalemia was modeled by increasing the extracellular potassium concentration  $[K^+]_o$  from 4.5 mM (in the NZ) to 14.5 mM (in the IC). Acidosis was represented by reducing the maximal conductance of INa and ICaL by 25% (in the IC), along with a 3.4 mV positive voltage shift in INa current kinetics. The effects of anoxia were modeled by lowering intracellular adenosine triphosphate (ATP) concentration from 10 mM (in the NZ) to 3 mM (in the IC), influencing ATP-dependent potassium (IKatp) and ICaL currents. GJ remodeling was simulated by a 99.5% reduction in connexin 43 (Cx43)-mediated GJs, while 100% of GJs remained in the NZ, at 666 mS/cm<sup>2</sup> (21). To assign parameter values within the BZ, we defined a smooth transition from IC to NZ values using the mapping  $f(x, y) = f_0(x - n \sin(by))$ , where

$$f_0(z) = \frac{a_{NZ} + a_{IC}}{2} + \frac{a_{NZ} - a_{IC}}{2} \tanh\left(\frac{z + L/2}{L/2}\right).$$

Here,  $a_{NZ}$  and  $a_{IC}$  represent the parameter values in the NZ and IC, respectively. The parameters  $b$ ,  $n$ , and  $L$  control the frequency, depth, and width of the finger-like protrusions in the BZ.

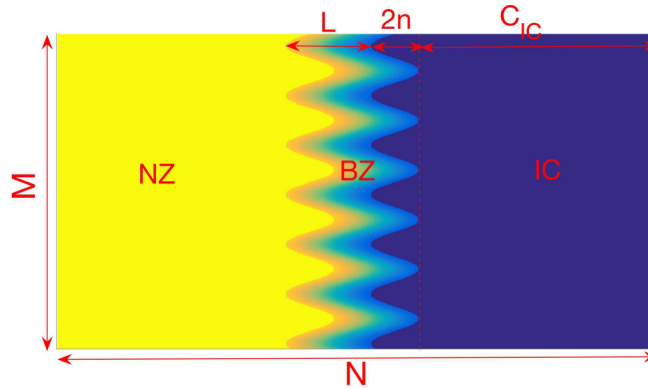


Figure 2: Display of NZ, BZ (with “fingers”-like geometry) and IC, where  $b$ ,  $n$ , and  $L$  control the frequency, depth, and width of the “fingers” respectively.

## Numerical scheme and pacing protocol

To solve the large system of differential equations presented in Eqs 1 - 8, we employed a time-splitting method. In this approach, we updated potentials (such as  $\phi_i$ ,  $\phi_e$ ,  $\phi_c$ ,  $\phi_{ec}$ ) and ion concentrations ( $C_{i,k}$ ,  $C_{e,k}$ ,  $C_{c,k}$ ,  $C_{ec,k}$ ) in the first substep, while gating variables were updated in the second substep. The nonlinear components (GHK diffusive currents, ionic currents, and gating kinetics) were linearized using the corresponding potentials and concentrations from the previous time step. These were then handled using a backward-Euler type discretization along with the linear components. The system was solved using a direct method implemented in MATLAB.

We performed numerical simulations on a lattice consisting of  $M$  by  $N$  cells with a time step of 0.01 ms, where  $M = 40$  and  $N = 100$ . Initially, all gating variables, ionic concentrations, and potentials were set to steady state. Conduction was triggered by excitatory current pulses with an amplitude of 0.15  $\mu A$  and a duration of 2 ms, applied to all cells from either the left-hand

side or the top of the lattice to initiate conduction in the longitudinal or transverse direction. Periodic pacing with a basic cycle length (BCL) of 500 ms was applied as necessary to establish a steady state, and the electrochemical properties of the last two beats were recorded.

The wavefront of typical AP propagation was characterized by the spatial point where the side transmembrane potential ( $V_m$ ) exceeded -30 mV, along with a positive temporal derivative ( $\frac{\partial V_m}{\partial t} > 0$ ). This criterion was used to differentiate normal APs from small-amplitude APs (SAP) (14, 21). SAP, as defined in (21), is a unique type of AP that can propagate through cardiac tissue despite having a reduced amplitude (maximum  $V_m = -40$  mV) and a significantly shorter action potential duration (APD), which is the period between the initiation of the AP (depolarization) and its return to the resting membrane potential (repolarization). Activation was monitored by identifying the earliest activation time (EAT) in each column or row of the  $M$  by  $N$  lattice. The CV in the longitudinal ( $CV_L$ ) and transverse direction ( $CV_T$ ) were computed by performing linear regression of the EAT over 20-80% of the lattice to reduce boundary effects. A CB was defined as the failure of the wavefront to reach the right-hand side of the lattice.

## RESULTS

In this section, we aim to explore the impact of EpC and multidomain electrodiffusion on cardiac dynamics. To achieve this, we presented a comparison between our previously developed bidomain model (14, 15, 21) and the multidomain electrodiffusion model, focusing on cardiac dynamics under EpC. We primarily investigated CV, AP morphology, propagation into the ischemic region, instability of planar front and dynamic changes in ionic concentrations. Each of these findings was explored using three specific distributions of ionic channels outlined in the Membrane dynamics Section. However, for CV, propagation into the ischemic region and instability of planar front—all of which are primarily governed by depolarization—the effects of localized IKi and ICaL are minimal. For this reason, the corresponding data are not shown. Additionally, we sought to elucidate the ionic mechanisms of EpC by analyzing dynamic changes in cleft ionic concentrations.

### Conduction velocity

We initiated our study by evaluating the effect of EpC on  $CV_L$  and  $CV_T$ , utilizing both bidomain (black) and electrodiffusion (red) models, with varying GJs. Figs. 3 and 4 depicted the  $CV_L$  and  $CV_T$ , respectively, as a function of  $d_{\text{cleft}}$  in the presence of low (0.5%) and normal (100%) GJ. Additionally, the INa current is localized to the cleft, whereas the IKi and ICaL currents are uniformly distributed along the membrane.

As shown in Fig. 3, both the bidomain and multidomain electrodiffusion models exhibit qualitatively similar behavior.  $CV_L$  exhibits a biphasic behavior with respect to  $d_{\text{cleft}}$  when GJ is 0.5%. In contrast, when GJ is 100%,  $CV_L$  decreases as  $d_{\text{cleft}}$  decreases. However, a distinction between the two models emerges when the cleft is sufficiently narrow, signifying strong EpC. Specifically, with 0.5% GJ coupling, the multidomain electrodiffusion model supports normal longitudinal conduction at  $d_{\text{cleft}} = 4$  nm, while the bidomain model exhibits SAP. At  $d_{\text{cleft}} = 8.4$  nm, the  $CV_L$  increases from 5 cm/s in the bidomain model to 7 cm/s in the electrodiffusion model. Moreover, with 100% GJ, the electrodiffusion model maintains normal conduction at  $d_{\text{cleft}} = 5$  nm, while the bidomain model experiences CB. Additionally,  $CV_L$  increases from 20 cm/s in the bidomain model to 25 cm/s in the electrodiffusion model when  $d_{\text{cleft}} = 8$  nm.

In Fig. 4, both models depict a decrease in  $CV_T$  as  $d_{\text{cleft}}$  diminishes, with both eventually showing CB at extremely small cleft widths. However, distinctions between the two models emerge when EpC becomes moderate to strong. For instance, at 0.5% GJ, the electrodiffusion model exhibits normal transverse propagation at  $d_{\text{cleft}} = 20$  nm and 50 nm, while the bidomain model shows CB. Moreover, for  $d_{\text{cleft}} > 50$  nm, the electrodiffusion model displays a slight increase in  $CV_T$  compared to the bidomain model. At 100% GJ, the electrodiffusion model demonstrates regular transverse propagation, whereas the bidomain model displays CB at  $d_{\text{cleft}} = 8$  nm and 12 nm. Notably, at  $d_{\text{cleft}} = 20$  nm, the electrodiffusion model exhibits an enhanced  $CV_T$  compared to the bidomain model. In summary, our findings suggest that moderate to strong EpC, combined with  $\text{Na}^+$  ion electrodiffusion, can enhance CV and decrease the likelihood of CB when INa currents are spatially localized.

### Action potential morphology

We proceeded to investigate how EpC influences AP morphology for both models. To emphasize the differences between the two models, we plotted the time profiles of  $V_m$  for a single cell within a 40 by 100 lattice as the AP propagates longitudinally. Specifically, we focused on the individual localizations of the INa (Fig. 5), ICaL (Fig. 6), and IKi (Fig. 7) channels with GJ at 0.5% (left panel) and 100% (right panel). Our results showed that the differences in AP morphology between the two models are consistent in both the longitudinal and transverse directions. Therefore, we only presented the data for the longitudinal direction.

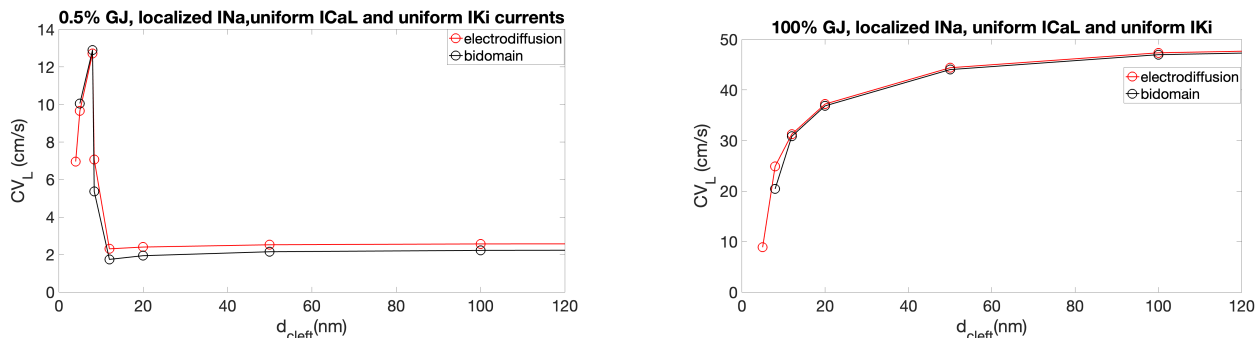


Figure 3:  $CV_L$  as a function of  $d_{cleft}$  at 0.5% GJ (left) and 100% GJ (right) when INa is localized. Electrodiffusion model shown in red; bidomain model in black.

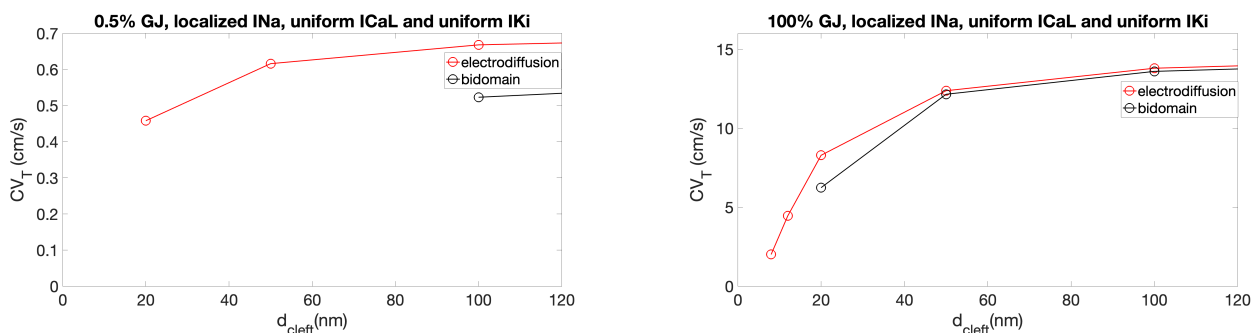


Figure 4:  $CV_T$  as a function of  $d_{cleft}$  at 0.5% GJ (left) and 100% GJ (right) when INa is localized. Electrodiffusion model shown in red; bidomain model in black.

### Localized INa channels

As shown in Fig. 5, notable differences between the electrodiffusion model (red) and the bidomain model (black) are observed in the depolarization phase of the AP for both 0.5% and 100% GJ. At  $d_{cleft} = 4$  nm (dotted) with 0.5% GJ and 6 nm (dotted) with 100% GJ, the  $V_m$  trace in the bidomain model exhibits SAP, whereas the electrodiffusion model maintains a normal AP. Furthermore, at  $d_{cleft} = 5$  nm (dashed) with 0.5% GJ, and 8 nm and 20 nm (dashed and solid) with 100% GJ, the bidomain model exhibits an AP characterized by a steep initial depolarization followed by a shallow one. In contrast, the electrodiffusion model presents an AP with a sharper upstroke phase. The differences between the two models during the upstroke phase are attributed to  $Na^+$  electrodiffusion, which reduces the ephaptic effects resulting from the localization of INa channels to the narrow cleft.

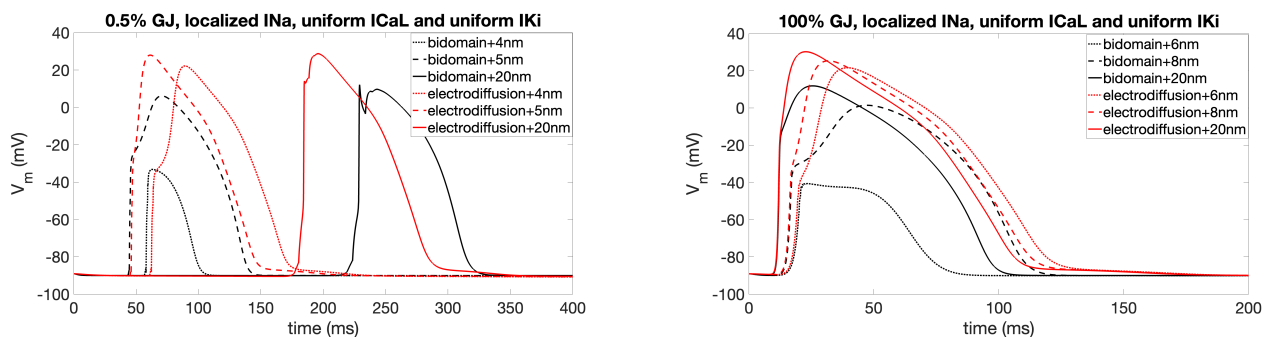


Figure 5:  $V_m$  traces at varying  $d_{cleft}$  during longitudinal AP propagation with localized INa: 0.5% GJ (left) and 100% GJ (right). Electrodiffusion model is shown in red, and the bidomain model in black.

## Localized ICaL channels

As shown in Fig. 6, significant differences between the electrodiffusion model and the bidomain model are observed in the APD values for both 0.5% and 100% GJ. Notably, APD values remain constant in the bidomain model as  $d_{\text{cleft}}$  changes, whereas in the electrodiffusion model, APD decreases significantly with decreasing  $d_{\text{cleft}}$ . The observed differences in APD between the two models are attributed to  $\text{Ca}^{2+}$  electrodiffusion, which enhances the ephaptic effects resulting from localization of ICaL channels to the narrow cleft.

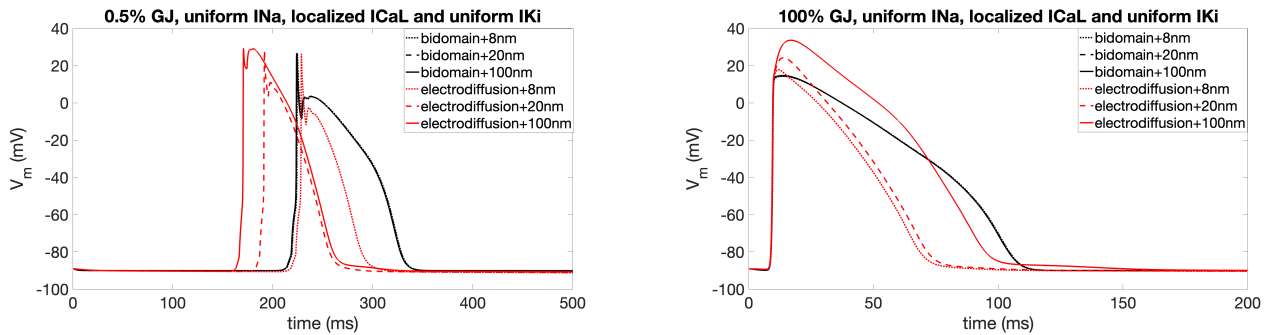


Figure 6:  $V_m$  traces at varying  $d_{\text{cleft}}$  during longitudinal AP propagation with localized ICaL: 0.5% GJ (left) and 100% GJ (right). Electrodiffusion model is shown in red, and the bidomain model in black.

## Localized IKi channels

As shown in Fig. 7, notable differences between the electrodiffusion and bidomain models are observed in the late repolarization and resting potential, corresponding to phase 4 of the AP, at both 0.5% and 100% GJ. Notably, at 0.5% GJ, CB is observed in the bidomain model but not in the electrodiffusion model. At 100% GJ,  $V_m$  traces remain unchanged in the bidomain model as  $d_{\text{cleft}}$  decreases. In contrast, variations in late repolarization and elevated resting potentials are observed in the electrodiffusion model at both levels of GJ. These differences are attributed to the electrodiffusion of  $\text{K}^{+}$  ions, which enhances the ephaptic effects caused by the localization of IKi channels to the narrow cleft.

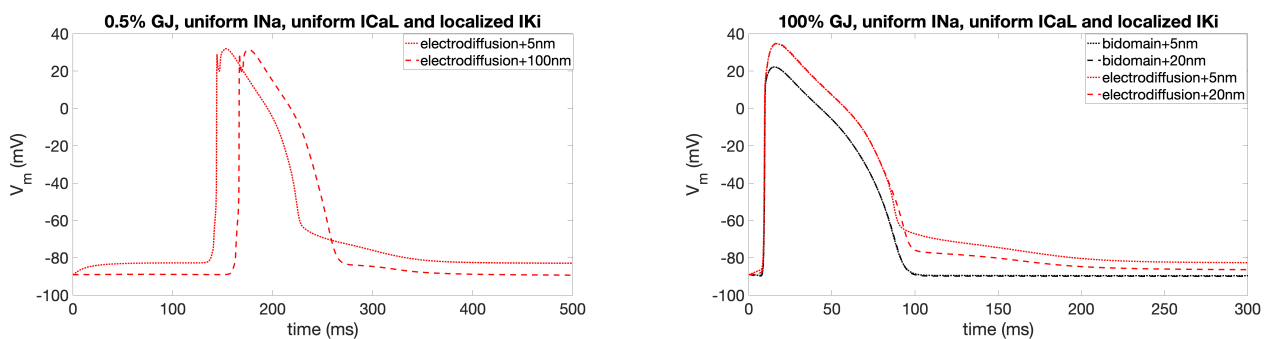


Figure 7:  $V_m$  traces at varying  $d_{\text{cleft}}$  during longitudinal AP propagation with localized IKi: 0.5% GJ (left) and 100% GJ (right). Electrodiffusion model is shown in red, and the bidomain model in black.

In conclusion, we highlighted the differences in AP morphology between the bidomain model and the electrodiffusion model when EpC is sufficiently strong. As shown in Figs. 5 - 7, discrepancies arise in the depolarization phase, APD values, late repolarization, and resting potential—key features influenced by the functions of INa, ICaL, and IKi. These findings suggest that ionic electrodiffusion plays a crucial role in shaping the morphology of the AP, especially in the presence of strong EpC. Specifically,  $\text{Na}^{+}$  electrodiffusion mitigates the ephaptic effects caused by the localization of INa channels to the narrow clefts by inducing a steep depolarization in the AP. Meanwhile,  $\text{Ca}^{2+}$  electrodiffusion further enhances the ephaptic effects resulting from the localization of ICaL channels to the narrow clefts by shortening APDs. Additionally,  $\text{K}^{+}$  electrodiffusion amplifies the ephaptic effects resulting from the localization of IKi channels to the narrow clefts by accelerating the late phase of repolarization and elevating resting potentials.

## Conduction across the ischemic region

In this section, we aim to illustrate how EpC, ionic electrodiffusion, and the geometry of the ischemic BZ influence propagation into the ischemic region. To achieve this, we sought to examine differences between the bidomain and electrodiffusion models in ephaptic conduction across a  $40 \times 100$  lattice, spanning from NZ to IC, as shown in Fig. 2. Here INa channels are localized, ICaL and IKi channels are uniformly distributed along the membrane. Our findings suggest that when EpC is either excessively strong or weak, there is no substantial disparity in AP propagation into the IC between the two models (data not shown). However, when EpC is at a moderate level, differences in AP propagation and morphology become evident, as shown in Figs. 8 and 9.

Fig. 8 presents snapshots of  $V_m$  for both electrodiffusion (A) and bidomain (B) models along the lattice into the IC, where  $d_{\text{cleft}} = 10$  nm,  $n = 10$ ,  $L = 20$ ,  $\text{Num}_{\text{col}} = 30$ , and  $b = 0.8$ . In this setting, the BZ has a complex geometry because  $n > 0$ . As shown in Fig. 8, ephaptic conduction successfully propagates into the IC in both models, but with distinct AP morphologies. Specifically, the electrodiffusion model shows a normal AP, while the bidomain model exhibits a SAP within the IC, characterized by a significant reduction in voltage amplitudes (-25 mV).

Fig. 9 shows snapshots of  $V_m$  for both the electrodiffusion (A) and bidomain (B) models along the lattice into the IC, with parameters  $d_{\text{cleft}} = 13$  nm,  $n = 0$ ,  $L = 20$ ,  $\text{Num}_{\text{col}} = 30$  and  $b = 1$ . Compared to Fig. 8, we varied the parameters  $b$ ,  $n$ , and  $d_{\text{cleft}}$  to demonstrate that the observed phenomena are not specific to a single parameter set, thereby highlighting the variability in both the data and the resulting propagation behaviors. In this configuration,  $n = 0$  signifies that the BZ has a simple geometry, with a direct transition from NZ to IC. As shown in Fig. 9A, ephaptic conduction is successful in the electrodiffusion model, while in the bidomain model (Fig. 9B), it fails to propagate into the IC. In summary, Figs. 8 and 9 demonstrate that  $\text{Na}^+$  electrodiffusion promotes propagation into ischemic tissue when EpC is moderate.

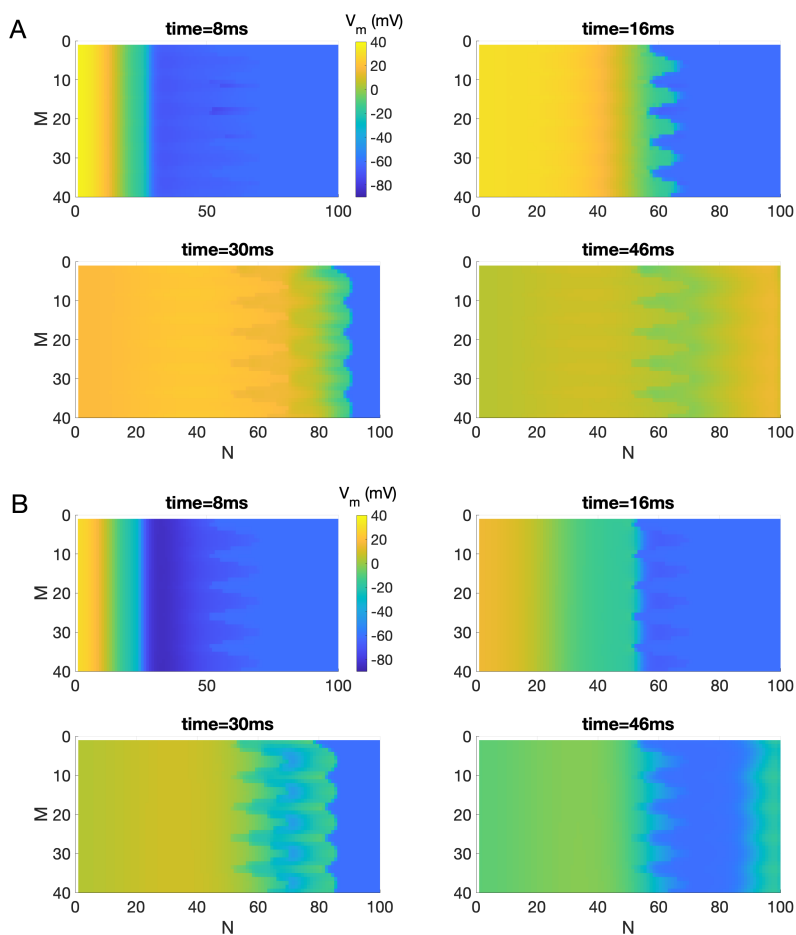


Figure 8: Snapshots of  $V_m$  illustrating longitudinal AP propagation across a  $40 \times 100$  lattice, spanning from NZ (left) to IC (right) (see Fig. 2), for the electrodiffusion (A) and bidomain (B) models, with  $d_{\text{cleft}} = 10$  nm and a complex BZ geometry ( $n = 10$ ,  $L = 20$ ,  $\text{Num}_{\text{col}} = 30$ , and  $b = 0.8$ ).

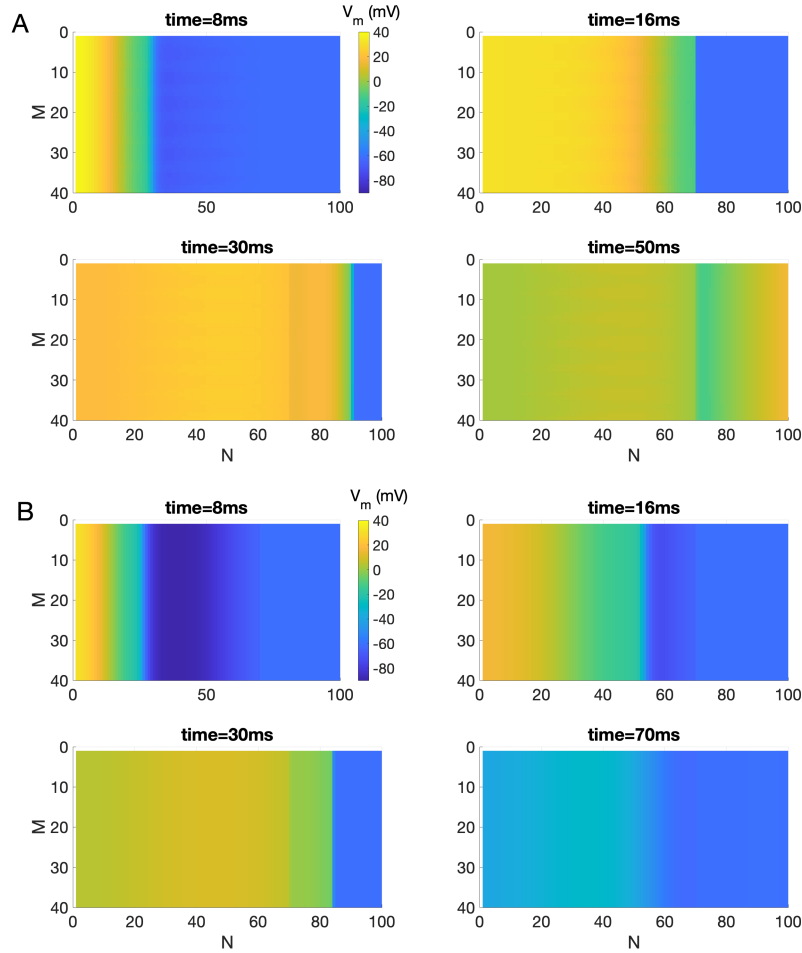


Figure 9: Snapshots of  $V_m$  illustrating longitudinal AP propagation across a  $40 \times 100$  lattice, spanning from NZ (left) to IC (right) (see Fig. 2), for the electrodiffusion (A) and bidomain (B) models, with  $d_{\text{cleft}} = 13$  nm and a simple BZ geometry ( $n = 0$ ,  $L = 20$ ,  $\text{Num}_{\text{col}} = 30$  and  $b = 1$ ).

## Instability of planar fronts

In this section, we investigated the impact of  $\text{Na}^+$  electrodiffusion and EpC on planar front instability, assuming that INa channels are localized, while ICaL and IKi channels are uniformly distributed along the membrane. In the bidomain model, the AP propagation manifests as irregular, zigzag-shaped wavefronts that travel through neighboring cells in a spatially heterogeneous manner across the lattice (Fig. 10A), occurring under conditions of 0.5% GJ and  $d_{\text{cleft}} = 10$  nm. In contrast, the electrodiffusion model maintains a stable planar front and does not exhibit this instability under the same conditions (Fig. 10B).

The persistence of the zigzag wavefront over time suggests that it arises from an instability of the planar front, as described in our earlier work (21, 47). We proposed that the instability arises from the coexistence of two conduction modes—ephaptic and GJ-mediated—that vary spatially in both the  $x$ - and  $y$ -directions. Specifically, a checkerboard pattern of ephaptic and GJ-mediated alternation gives rise to the instability of planar fronts. Electrodiffusion stabilizes wavefront propagation by modulating potential and ionic concentration gradients between neighboring cells, thereby suppressing the spatial heterogeneities that lead to zigzag or unstable fronts under low GJs with active ephaptic interactions.

## Dynamic changes in the ionic concentrations

In this section, we investigated the effect of EpC on the dynamic changes in ionic concentration using the electrodiffusion model, emphasizing one of its key advantages over the bidomain model. To gain a comprehensive understanding of these behaviors, we systematically varied the localization of INa, ICaL, and IKi channels individually. We monitored the ionic concentration in both the cleft and extracellular spaces within the lattice during the last two beats of periodic pacing. Given that GJs are set at 100% along the lattice, we selected a single cleft and extracellular space for plotting.

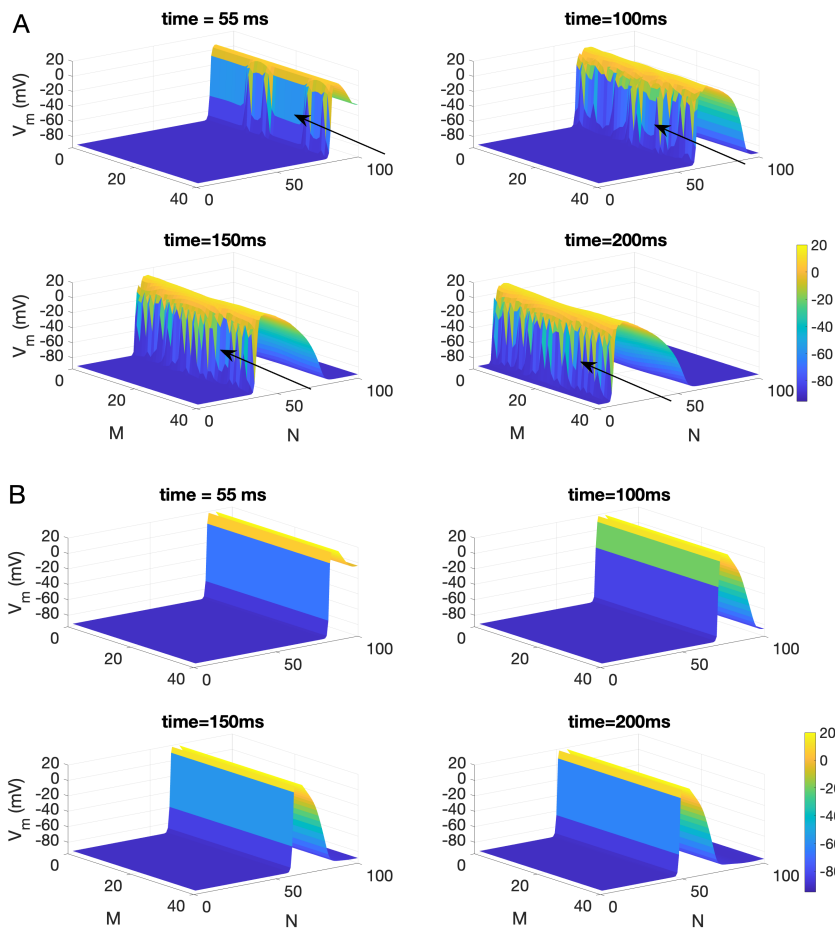


**Figure 10:** Snapshots of  $V_m$  showing planar front instability in the bidomain model (A), which is absent in the electrodiffusion model, under 0.5% GJ,  $d_{\text{cleft}} = 10$  nm, with localized  $I_{\text{Na}}$  and uniform  $I_{\text{CaL}}$  and  $I_{\text{Ki}}$  channels.

Figures 11 and 12 show the time profiles of extracellular (blue) and cleft (red) concentrations of  $\text{Na}^+$ ,  $\text{K}^+$ ,  $\text{Ca}^{2+}$ , and  $\text{Cl}^-$  with localized  $I_{\text{Na}}$  (A),  $I_{\text{CaL}}$  (B), and  $I_{\text{Ki}}$  (C) channels at  $d_{\text{cleft}} = 115$  nm and 5 nm, respectively, corresponding to near absence and strong presence of EpC. As shown in both figures, the extracellular (blue) and intracellular (data not shown) ionic concentrations exhibit minimal fluctuations. Additionally, Figs. 11B and C show relatively small changes in cleft  $[\text{Ca}^{2+}]$  and  $[\text{K}^+]$  at  $d_{\text{cleft}} = 115$  nm. Specifically, there is a slight decrease in cleft  $[\text{Ca}^{2+}]$  when  $I_{\text{CaL}}$  channels are localized, and a small increase in cleft  $[\text{K}^+]$  when  $I_{\text{Ki}}$  channels are localized.

In contrast, Fig. 12 shows more pronounced perturbations in the cleft ionic concentrations at  $d_{\text{cleft}} = 5$  nm. Specifically, when  $I_{\text{Na}}$  channels are localized, the narrow cleft results in a moderate reduction in cleft  $[\text{Na}^+]$  and  $[\text{Cl}^-]$ , along with noticeable fluctuations in cleft  $[\text{Ca}^{2+}]$ . Furthermore, when  $I_{\text{CaL}}$  channels are localized, there is a near depletion of  $\text{Ca}^{2+}$  ions in the cleft. Additionally, when  $I_{\text{Ki}}$  channels are localized, there are significant changes in cleft  $[\text{K}^+]$  and  $[\text{Ca}^{2+}]$ , with relatively minor changes in  $[\text{Na}^+]$  and  $[\text{Cl}^-]$ . In particular, cleft  $[\text{K}^+]$  increases substantially, reaching 8 mM.

In summary, our findings suggest that changes in extracellular ionic concentrations are minimal regardless of  $d_{\text{cleft}}$ . Furthermore, the ionic concentrations in the cleft space are only slightly perturbed when EpC is weak. However, strong EpC can dramatically alter the ionic concentrations in the cleft, which are closely related to the localization of ionic channels  $I_{\text{Na}}$ ,  $I_{\text{CaL}}$ , and  $I_{\text{Ki}}$ . Notably, there is a significant increase in  $[\text{K}^+]$  and near depletion of  $\text{Ca}^{2+}$  in the cleft, while changes in cleft  $[\text{Na}^+]$  are moderate. These findings may provide insight into the ionic mechanism of EpC, specifically the depletion of  $\text{Ca}^{2+}$  ions and/or the accumulation of  $\text{K}^+$  in the cleft.

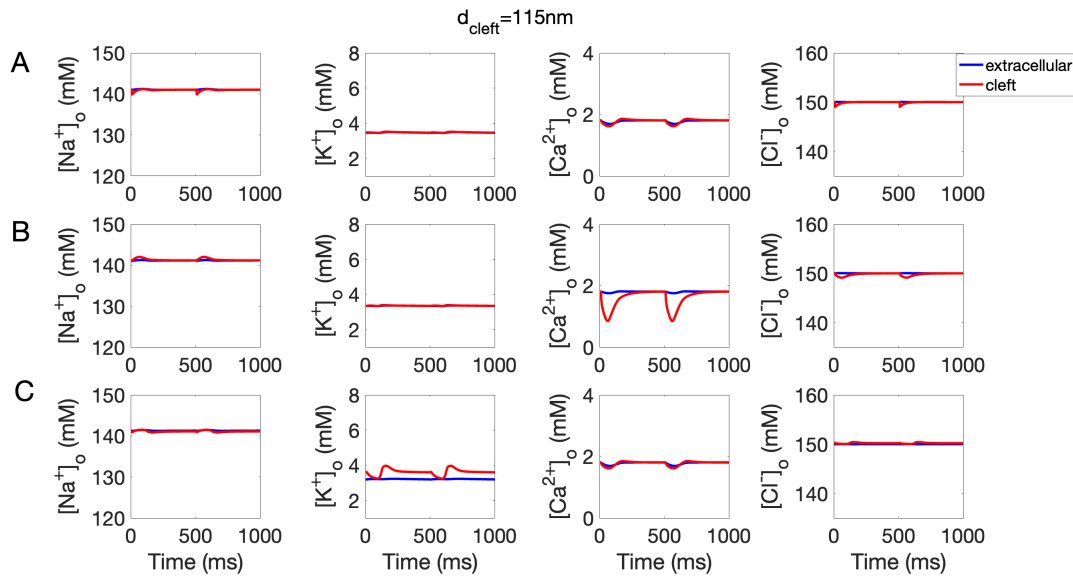


**Figure 11:** The time profiles of extracellular ( ) and cleft (red) concentrations of  $Na^+$ ,  $K^+$ ,  $Ca^{2+}$  and  $Cl^-$  with localized InA (A), ICaL (B), and IKi (C) channels at  $d_{cleft} = 115$  nm.

## DISCUSSION

In this paper, we explored the interplay between ionic electrodiffusion and EpC on cardiac dynamics, including AP propagation, morphology, and electrochemical properties in both healthy and ischemic hearts. To achieve this, we developed a 2D discrete multidomain electrodiffusion model that incorporates EpC. Our findings indicate that under strong EpC,  $Na^+$  electrodiffusion enhances CV, reduces the occurrence of CB, and sharpens the upstroke phase of the AP, while  $Ca^{2+}$  and  $K^+$  diffusion shorten the AP duration, alter the repolarization phase, and elevate the resting membrane potential. Additionally, when EpC is prominent,  $Na^+$  electrodiffusion helps stabilize AP propagation and promotes its spread into ischemic regions. Strong EpC also significantly alters ionic concentrations in the cleft, markedly increasing  $[K^+]$ , nearly depleting  $[Ca^{2+}]$ , and causing moderate changes in  $[Na^+]$ . This multidomain electrodiffusion model provides valuable insights into the mechanisms of EpC in the heart.

Our model is the first physiologically accurate 2D model that includes the electrodiffusion of all major ions in conjunction with EpC. Furthermore, our model simulates ionic transport and accumulation across multiple compartments at both the subcellular and cellular levels, revealing qualitative and quantitative features that differ from previous one-dimensional studies where ion electrodiffusion is limited to the cleft. This model can be used to investigate the impact of EpC on arrhythmogenesis in the ischemic heart, where ionic electrodiffusion plays a critical role. Ultimately, our discrete electrodiffusion model provides substantial advantages over continuous models by accurately capturing the slow and discontinuous nature of AP propagation in the diseased heart.

We highlighted key differences between the multidomain electrodiffusion model and the bidomain model in cardiac functions, including AP kinetics, morphology, and electrochemical properties in both healthy and ischemic hearts. These findings underscore the influence of multidomain electrodiffusion of multiple ions and its interaction with EpC on cardiac activity, providing a foundation for investigating their roles in arrhythmogenesis, which earlier models could not achieve. Myocardial ischemia, caused by severe coronary artery obstruction, leads to significant electrochemical gradients along with notable physiological and anatomical changes (48–50), which can potentially result in cardiac arrhythmias (51–53). In particular, reduced and remodeled GJs are prominent features in all ischemia-related heart diseases (48–50). These conditions provides an ideal setting for the interaction between ionic electrodiffusion and EpC, as both are crucial. Our innovative approach allows for the interaction between EpC and electrodiffusion in shaping cardiac dynamics and the exploration of various biophysical phenomena under both healthy and ischemic conditions.

The clinical relevance of ionic electrodiffusion becomes apparent in various conditions such as heart failure, congenital channelopathies, and acquired arrhythmias. For example, abnormal expression and function of ion channels can lead to disrupted repolarization and consequently induce arrhythmias such as atrial fibrillation (AF) and ventricular tachycardia (VT) (54, 55). AF, which increases the risk of stroke and heart failure, has been associated with alterations in  $K^+$  channel function (55–57), particularly in the atrial myocardium. Moreover, genetic mutations affecting the electric properties of ion channels are

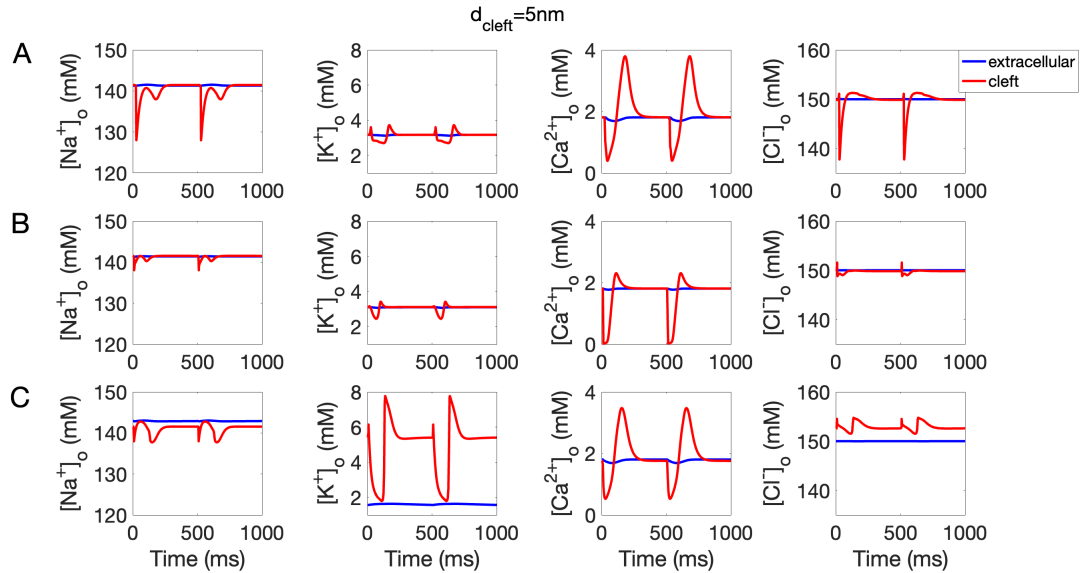


Figure 12: The time profiles of extracellular (blue) and cleft (red) concentrations of  $\text{Na}^+$ ,  $\text{K}^+$ ,  $\text{Ca}^{2+}$  and  $\text{Cl}^-$  with localized  $\text{INa}$  (A),  $\text{ICaL}$  (B), and  $\text{IKi}$  (C) channels at  $d_{\text{cleft}} = 5 \text{ nm}$ .

increasingly recognized as significant contributors to arrhythmia susceptibility. For instance, mutations in the gene encoding the cardiac sodium channel, *SCN5A*, can lead to Brugada syndrome (58, 59), long QT syndrome (60) and cardiac disorders (61), both characterized by dangerous arrhythmic potential. These conditions highlight the importance of genetic screening and personalized approaches in managing patients with inherited arrhythmias stemming from ionic electrodiffusion abnormalities. On the other hand, exploring the underlying mechanisms of EpC in cardiac conduction and arrhythmogenesis is of critical clinical importance. Studies indicate that EpC can help restore cardiac conduction when GJs are impaired. Specifically, research has shown that EpC enhances CV (11, 12, 16, 21–23), reduces CB (14, 21), and ultimately terminates reentry (15) in ischemic heart models with reduced GJs. Gaining a mechanistic understanding of EpC can drive the development of new anti-arrhythmic drugs and therapies to tackle various cardiovascular issues.

Our ongoing investigation also reveals several limitations. First, we have neglected the intricate geometry of individual cells and the structure of the intercalated disc, both of which may influence ionic dynamics and arrhythmogenesis in cardiac tissue. While accounting for these features would significantly increase the complexity of the multidomain electrodiffusion model—and thus the computational burden—it remains an important direction for future research. Another limitation is the omission of the branching structure of cardiac tissue, which could impact EpC and alter propagation dynamics. Although incorporating this anatomical detail would add further computational cost, it represents a meaningful objective for future model development. A final limitation concerns model validation. We validated our electrodiffusion framework by comparing CV measurements with results from our previously published bidomain model (14, 21) as well as other studies (23, 62). Additionally, the “finger-like” geometry of the ischemic region used in our simulations is based on experimental data from Dr. Talkachova’s lab (42). However, the complexity of EpC and lack of direct experimental data of ion concentrations in the cleft space underscore the challenges in this field—highlighting the crucial role of mathematical modeling. To address these limitations, we are actively collaborating with experimentalists to apply our electrodiffusion model in studying how extracellular and cleft-space ion concentrations influence CV. Furthermore, we are currently employing our 2D electrodiffusion model to explore the interaction between ephaptic coupling and multidomain electrodiffusion in cardiac arrhythmias—an important step toward understanding the fundamental mechanisms of EpC in arrhythmogenesis.

## CONCLUSION

In this paper, we explored the interplay between ionic electrodiffusion and EpC on cardiac dynamics, including AP propagation, morphology, and electrochemical properties in both healthy and ischemic hearts. To achieve this, we developed a 2D discrete multidomain electrodiffusion model that incorporates EpC. Our findings indicate that under strong EpC,  $\text{Na}^+$  electrodiffusion enhances CV, reduces the occurrence of CB, and sharpens the upstroke phase of the AP, while  $\text{Ca}^{2+}$  and  $\text{K}^+$  diffusion shorten the AP duration, alter the repolarization phase, and elevate the resting membrane potential. Additionally, when EpC is prominent,

$\text{Na}^+$  electrodiffusion helps stabilize AP propagation and promotes its spread into ischemic regions. Strong EpC also significantly alters ionic concentrations in the cleft, markedly increasing  $[\text{K}^+]$ , nearly depleting  $[\text{Ca}^{2+}]$ , and causing moderate changes in  $[\text{Na}^+]$ . This multidomain electrodiffusion model provides valuable insights into the mechanisms of EpC in the heart.

## AUTHOR CONTRIBUTIONS

Ning Wei developed the mathematical model. Ning Wei and Yoichiro Mori jointly designed the numerical experiments. Ning Wei performed the numerical simulations, analyzed the results, and wrote and edited the manuscript.

## ACKNOWLEDGMENTS

This study is supported by NSF grants DMS-2327184 and DMS-2152115 awarded to Ning Wei, as well as the Simons Collaboration Grant for Mathematicians 855881 to Ning Wei. Additionally, this study is also supported by the Simons Foundation through the Math+X Chair Fund awarded to Yoichiro Mori.

## REFERENCES

1. Shaw, R. M., and Y. Rudy, 1997. Ionic mechanisms of propagation in cardiac tissue roles of the sodium and l-type calcium currents during reduced excitability and decreased gap junction coupling. *Circ. Res.* 81:727–741.
2. Vaidya, D., H. S. Tamaddon, C. W. Lo, S. M. Taffet, M. Delmar, G. E. Morley, and J. Jalife, 2001. Null mutation of connexin43 causes slow propagation of ventricular activation in the late stages of mouse embryonic development. *Circ. Res.* 88:1196–1202.
3. Beauchamp, P., C. Choby, T. Desplantez, K. de Peyer, K. Green, K. A. Yamada, R. Weingart, J. E. Saffitz, and A. G. Kléber, 2004. Electrical propagation in synthetic ventricular myocyte strands from germline connexin43 knockout mice. *Circ. Res.* 95:170–178.
4. Beauchamp, P., T. Desplantez, M. L. McCain, W. Li, A. Asimaki, G. Rigoli, K. K. Parker, J. E. Saffitz, and A. G. Kleber, 2012. Electrical coupling and propagation in engineered ventricular myocardium with heterogeneous expression of connexin43. *Circ. Res.* 110:1445–1453.
5. Rohr, S., 2004. Role of gap junctions in the propagation of the cardiac action potential. *Cardiovasc. Res.* 62:309–322.
6. Danik, S. B., F. Liu, J. Zhang, H. J. Suk, G. E. Morley, G. I. Fishman, and D. E. Gutstein, 2004. Modulation of cardiac gap junction expression and arrhythmic susceptibility. *Circ. Res.* 95:1035–1041.
7. Yao, J.-A., D. E. Gutstein, F. Liu, G. I. Fishman, and A. L. Wit, 2003. Cell coupling between ventricular myocyte pairs from connexin43-deficient murine hearts. *Circ. Res.* 93:736–743.
8. Sperelakis, N., and J. E. Mann, 1977. Evaluation of electric field changes in the cleft between excitable cells. *J. Theor. Biol.* 64:71–96.
9. Sperelakis, N., 2002. An electric field mechanism for transmission of excitation between myocardial cells. *Circ. Res.* 91:985–987.
10. Copene, E. D., and J. P. Keener, 2008. Ephaptic coupling of cardiac cells through the junctional electric potential. *J. Math. Biol.* 57:265–284.
11. Lin, J., and J. P. Keener, 2010. Modeling electrical activity of myocardial cells incorporating the effects of ephaptic coupling. *Proc. Natl. Acad. Sci.* 107:20935–20940.
12. Lin, J., and J. P. Keener, 2013. Ephaptic coupling in cardiac myocytes. *IEEE Trans. Biomed. Eng.* 60:576–582.
13. Mori, Y., G. I. Fishman, and C. S. Peskin, 2008. Ephaptic conduction in a cardiac strand model with 3D electrodiffusion. *Proc. Natl. Acad. Sci.* 105:6463–6468.
14. Wei, N., and E. G. Tolkacheva, 2020. Interplay between ephaptic coupling and complex geometry of border zone during acute myocardial ischemia: Effect on arrhythmogeneity. *Chaos: An Interdisciplinary Journal of Nonlinear Science* 30.

15. Wei, N., and E. G. Tolkacheva, 2022. Mechanisms of arrhythmia termination during acute myocardial ischemia: Role of ephaptic coupling and complex geometry of border zone. *PLoS one* 17:e0264570.
16. George, S. A., M. Bonakdar, M. Zeitz, R. V. Davalos, J. W. Smyth, and S. Poelzing, 2016. Extracellular sodium dependence of the conduction velocity-calcium relationship: evidence of ephaptic self-attenuation. *American Journal of Physiology-Heart and Circulatory Physiology* 310:H1129–H1139.
17. George, S. A., G. Hoeker, P. J. Calhoun, M. Entz, T. B. Raisch, D. R. King, M. Khan, C. Baker, R. G. Gourdie, J. W. Smyth, M. S. Nielsen, and S. Poelzing, 2019. Modulating cardiac conduction during metabolic ischemia with perfusate sodium and calcium in guinea pig hearts. *American Journal of Physiology-Heart and Circulatory Physiology* 316:H849–H861.
18. Hoeker, G. S., C. C. James, A. N. Tegge, R. G. Gourdie, J. W. Smyth, and S. Poelzing, 2020. Attenuating loss of cardiac conduction during no-flow ischemia through changes in perfusate sodium and calcium. *American Journal of Physiology-Heart and Circulatory Physiology* 319:H396–H409.
19. Veeraghavan, R., J. Lin, G. S. Hoeker, J. P. Keener, R. G. Gourdie, and S. Poelzing, 2015. Sodium channels in the Cx43 gap junction perinexus may constitute a cardiac ephapse: an experimental and modeling study. *Pflügers Archiv-European Journal of Physiology* 467:2093–2105.
20. Tsumoto, K., T. Ashihara, N. Naito, T. Shimamoto, A. Amano, Y. Kurata, and Y. Kurachi, 2020. Specific decreasing of Na<sup>+</sup> channel expression on the lateral membrane of cardiomyocytes causes fatal arrhythmias in Brugada syndrome. *Scientific reports* 10:1–16.
21. Wei, N., Y. Mori, and E. G. Tolkacheva, 2016. The dual effect of ephaptic coupling on cardiac conduction with heterogeneous expression of connexin 43. *Journal of theoretical biology* 397:103–114.
22. Hand, P. E., B. E. Griffith, and C. S. Peskin, 2009. Deriving macroscopic myocardial conductivities by homogenization of microscopic models. *Bull. Math. Biol.* 71:1707–1726.
23. Hand, P. E., and C. S. Peskin, 2010. Homogenization of an electrophysiological model for a strand of cardiac myocytes with gap-junctional and electric-field coupling. *Bull. Math. Biol.* 72:1408–1424.
24. Gutstein, D. E., G. E. Morley, H. Tamaddon, D. Vaidya, M. D. Schneider, J. Chen, K. R. Chien, H. Stuhlmann, and G. I. Fishman, 2001. Conduction slowing and sudden arrhythmic death in mice with cardiac-restricted inactivation of connexin43. *Circ. Res.* 88:333–339.
25. Kucera, J. P., A. G. Kléber, and S. Rohr, 1998. Slow conduction in cardiac tissue, II: effects of branching tissue geometry. *Circulation research* 83:795–805.
26. Wei, X., S. Yohannan, and J. R. Richards, 2019. Physiology, cardiac repolarization dispersion and reserve .
27. Steenbergen, C., E. Murphy, L. Levy, and R. E. London, 1987. Elevation in cytosolic free calcium concentration early in myocardial ischemia in perfused rat heart. *Circulation research* 60:700–707.
28. Steenbergen, C., T. Fralix, and E. Murphy, 1993. Role of increased cytosolic free calcium concentration in myocardial ischemic injury. *Basic research in cardiology* 88:456–470.
29. Cascio, W. E., 2001. Myocardial ischemia: what factors determine arrhythmogenesis? *Journal of cardiovascular electrophysiology* 12:726–729.
30. Shine, K. I., 1981. Myocardial ischemia: ionic events in ischemia and anoxia. *The American Journal of Pathology* 102:256.
31. Cascio, W. E., T. A. Johnson, and L. S. Gettes, 1995. Electrophysiologic changes in ischemic ventricular myocardium: I. Influence of ionic, metabolic, and energetic changes. *Journal of cardiovascular electrophysiology* 6:1039–1062.
32. Hodgkin, A. L., and A. F. Huxley, 1952. A quantitative description of membrane current and its application to conduction and excitation in nerve. *The Journal of physiology* 117:500.
33. Hand, P. E., and B. E. Griffith, 2010. Adaptive multiscale model for simulating cardiac conduction. *Proceedings of the National Academy of Sciences* 107:14603–14608.

34. Hand, P. E., and B. E. Griffith, 2011. Empirical study of an adaptive multiscale model for simulating cardiac conduction. *Bulletin of mathematical biology* 73:3071–3089.
35. Moise, N., H. L. Struckman, C. Dagher, R. Veeraraghavan, and S. H. Weinberg, 2021. Intercalated disk nanoscale structure regulates cardiac conduction. *Journal of General Physiology* 153:e202112897.
36. Livshitz, L. M., and Y. Rudy, 2007. Regulation of Ca<sup>2+</sup> and electrical alternans in cardiac myocytes: role of CAMKII and repolarizing currents. *Am. J. Physiol. Heart Circ. Physiol.* 292:H2854–H2866.
37. Cohen, S. A., and L. K. Levitt, 1993. Partial characterization of the rH1 sodium channel protein from rat heart using subtype-specific antibodies. *Circulation Research* 73:735–742.
38. Cohen, S. A., 1996. Immunocytochemical Localization of rH1 Sodium Channel in Adult Rat Heart Atria and Ventricle Presence in Terminal Intercalated Disks. *Circulation* 94:3083–3086.
39. Rohr, S., R. Fluckiger, and S. Cohen, 1999. Immunocytochemical localization of sodium and calcium channels in cultured neonatal rat ventricular cardiomyocytes. In BIOPHYSICAL JOURNAL. BIOPHYSICAL SOCIETY 9650 ROCKVILLE PIKE, BETHESDA, MD 20814-3998 USA, volume 76, A366–A366.
40. Maier, S. K., R. E. Westenbroek, K. A. Schenkman, E. O. Feigl, T. Scheuer, and W. A. Catterall, 2002. An unexpected role for brain-type sodium channels in coupling of cell surface depolarization to contraction in the heart. *Proc. Natl. Acad. Sci.* 99:4073–4078.
41. Veeraraghavan, R., J. Lin, J. P. Keener, R. Gourdie, and S. Poelzing, 2016. Potassium channels in the Cx43 gap junction perinexus modulate ephaptic coupling: an experimental and modeling study. *Pflügers Archiv-European Journal of Physiology* 468:1651–1661.
42. Smith, R. M., A. J. Black, S. S. Velamakanni, T. Akkin, and E. G. Tolkacheva, 2012. Visualizing the complex 3D geometry of the perfusion border zone in isolated rabbit heart. *Appl. Opt.* 51:2713–2721.
43. Bernus, O., C. W. Zemlin, R. M. Zaritsky, S. F. Mironov, and A. M. Pertsov, 2005. Alternating conduction in the ischaemic border zone as precursor of reentrant arrhythmias: a simulation study. *Europace* 7:S93–S104.
44. Shaw, R. M., and Y. Rudy, 1997. Electrophysiologic effects of acute myocardial ischemia: a theoretical study of altered cell excitability and action potential duration. *Cardiovasc. Res.* 35:256–272.
45. Smith, J., C. Green, N. Peters, S. Rothery, and N. Severs, 1991. Altered patterns of gap junction distribution in ischemic heart disease. An immunohistochemical study of human myocardium using laser scanning confocal microscopy. *The American journal of pathology* 139:801.
46. Wang, X., and A. M. Gerdes, 1999. Chronic pressure overload cardiac hypertrophy and failure in guinea pigs: III. Intercalated disc remodeling. *J. Mol. Cell. Cardiol.* 31:333–343.
47. Mori, Y., and H. Matano, 2016. Stability of front solutions of the bidomain equation. *Communications on Pure and Applied Mathematics* 69:2364–2426.
48. Janse, M. J., and A. L. Wit, 1989. Electrophysiological mechanisms of ventricular arrhythmias resulting from myocardial ischemia and infarction. *Physiological reviews* 69:1049–1169.
49. Coronel, R., F. Wilms-Schopman, T. Opthof, J. Cinca, J. Fiolet, and M. J. Janse, 1992. Reperfusion arrhythmias in isolated perfused pig hearts. Inhomogeneities in extracellular potassium, ST and TQ potentials, and transmembrane action potentials. *Circ. Res.* 71:1131–1142.
50. Shaw, R. M., and Y. Rudy, 1997. Electrophysiologic Effects of Acute Myocardial Ischemia A Mechanistic Investigation of Action Potential Conduction and Conduction Failure. *Circulation Research* 80:124–138.
51. Luqman, N., R. J. Sung, C.-L. Wang, and C.-T. Kuo, 2007. Myocardial ischemia and ventricular fibrillation: pathophysiology and clinical implications. *International journal of cardiology* 119:283–290.
52. Lazzara, R., N. El-Sherif, R. Hope, and B. Scherlag, 1978. Ventricular arrhythmias and electrophysiological consequences of myocardial ischemia and infarction. *Circulation research* 42:740–749.

53. Reimer, K. A., and R. E. Ideker, 1987. Myocardial ischemia and infarction: anatomic and biochemical substrates for ischemic cell death and ventricular arrhythmias. *Human pathology* 18:462–475.
54. Locati, E. T., G. Bagliani, F. Cecchi, H. Johny, M. Lunati, and C. Pappone, 2019. Arrhythmias due to inherited and acquired abnormalities of ventricular repolarization. *Cardiac Electrophysiology Clinics* 11:345–362.
55. Lei, M., S. C. Salvage, A. P. Jackson, and C. L.-H. Huang, 2024. Cardiac arrhythmogenesis: roles of ion channels and their functional modification. *Frontiers in Physiology* 15:1342761.
56. Burg, S., and B. Attali, 2021. Targeting of potassium channels in cardiac arrhythmias. *Trends in Pharmacological Sciences* 42:491–506.
57. Diness, J. G., B. H. Bentzen, U. S. Sørensen, and M. Grønnet, 2015. Role of calcium-activated potassium channels in atrial fibrillation pathophysiology and therapy. *Journal of cardiovascular pharmacology* 66:441–448.
58. Kyndt, F., V. Probst, F. Potet, S. Demolombe, J.-C. Chevallier, I. Baro, J.-P. Moisan, P. Boisseau, J.-J. Schott, D. Escande, et al., 2001. Novel SCN5A mutation leading either to isolated cardiac conduction defect or Brugada syndrome in a large French family. *Circulation* 104:3081–3086.
59. Shin, D.-J., Y. Jang, H.-Y. Park, J. E. Lee, K. Yang, E. Kim, Y. Bae, J. Kim, J. Kim, S. S. Kim, et al., 2004. Genetic analysis of the cardiac sodium channel gene SCN5A in Koreans with Brugada syndrome. *Journal of human genetics* 49:573–578.
60. Rivolta, I., H. Abriel, M. Tateyama, H. Liu, M. Memmi, P. Vardas, C. Napolitano, S. G. Priori, and R. S. Kass, 2001. Inherited Brugada and long QT-3 syndrome mutations of a single residue of the cardiac sodium channel confer distinct channel and clinical phenotypes. *Journal of Biological Chemistry* 276:30623–30630.
61. Li, W., L. Yin, C. Shen, K. Hu, J. Ge, and A. Sun, 2018. SCN5A variants: association with cardiac disorders. *Frontiers in physiology* 9:1372.
62. Kucera, J. P., S. Rohr, and Y. Rudy, 2002. Localization of sodium channels in intercalated disks modulates cardiac conduction. *Circ. Res* 91:1176–1182.